Chemical Science

ROYAL SOCIETY OF CHEMISTRY

EDGE ARTICLE

View Article Online
View Journal | View Issue

Cite this: *Chem. Sci.*, 2024, **15**, 15160

All publication charges for this article have been paid for by the Royal Society of Chemistry

δ-Bonding modulates the electronic structure of formally divalent nd^1 rare earth arene complexes†

Ross E. MacKenzie, [ab] Tomáš Hajdu, [bd] John A. Seed, [ab] George F. S. Whitehead, [b] Ralph W. Adams, [b] Nicholas F. Chilton, [bc] David Collison, [bd] Eric J. L. McInnes [bd] and Conrad A. P. Goodwin *[ab]

Received 7th May 2024
Accepted 28th July 2024

DOI: 10.1039/d4sc03005b

rsc.li/chemical-science

Landmark advances in rare earth (RE) chemistry have shown that divalent complexes can be isolated with non-Aufbau 4f^n{5d/6s}^{1} electron configurations, facilitating remarkable bonding motifs and magnetic properties. We report a series of divalent bis-tethered arene complexes, [RE(NHAr^{iPr_6})$_2$] (**2RE**; RE = Sc, Y, La, Sm, Eu, Tm, Yb; NHAr^{iPr_6} = {N(H)C$_6$H$_3$-2,6-(C$_6$H$_2$-2,4,6-*i*Pr$_3$)$_2$}). Fluid solution EPR spectroscopy gives g_{iso} < 2.002 for **2Sc**, **2Y**, and **2La**, consistent with formal nd^1 configurations, calculations reveal metal–arene δ-bonding *via* mixing of nd$_{(x^2-y^2)}$ valence electrons into arene π* orbitals. Experimental and calculated EPR and UV-Vis-NIR spectroscopic properties for **2Y** show that minor structural changes markedly alter the metal d$_{(x^2-y^2)}$ contribution to the SOMO. This contrasts 4f^n{5d/6s}^{1} complexes where the valence d-based electron resides in a non-bonding orbital. Complexes **2Sm**, **2Eu**, **2Tm**, and **2Yb** contain highly-localised 4f^{n+1} ions with no appreciable metal–arene bonding by density functional calculations. These results show that the physicochemical properties of divalent rare earth arene complexes with both formal nd^1 and 4f^{n+1} configurations are nuanced, may be controlled through ligand modification, and require a multi-pronged experimental and theoretical approach to fully rationalise.

Introduction

A hallmark of trivalent lanthanide ions is the relative insensitivity of valence 4f-orbitals to the coordination environment. While this gives rise to useful physical and optical properties, such as their narrow optical emission profiles and large magnetic moments from their unquenched orbital angular momentum, the weakness of this interaction also inhibits the extent to which their properties may be tailored through molecular design. Advancements in divalent molecular rare earth and lanthanide (Sc, Y, La–Lu; collectively Ln henceforth) chemistry have shown that in coordination environments such as [Ln(Cp^R)$_3$]$^-$ or [Ln(Cp^R)$_2$] (Cp^R = substituted cyclopentadienide ligands), Ln(II) complexes can be isolated with 4f^{n}5d^1 or 4f^n{5d/6s}^{1} valence electron configurations, at least for La–Lu, while Sc and Y necessarily give 3d^1 or 4d^1 ions.[1–23] Further work shows these non-Aufbau ions can be exploited as potential qubit candidates,[15–17] exhibit record-setting magnetic properties,[18–20] and have produced the first examples of molecular Ln–Ln bonding outside of endohedral fullerenes.[20–22] Similar advancements have also been made with actinide elements.[24] However, with few exceptions, design strategies employed to isolate examples of these ions use geometries (*e.g.* C_{3h} or D_{5h}) that minimise or forbid, by symmetry, the mixing of 5d (or 5d/6s hybridised) valence electrons with ligand orbitals. This is useful in some applications,[15–17] but in analogy to the poor tunability of 4f-orbitals in Ln(III) ions, it limits the extent to which the electronic structures of 4f^{n}5d^1 or 4f^n{5d/6s}^{1} Ln(II) complexes may be controlled through ligand design.

Using ligand field principles commonplace in the d-block that also apply to 4f^{n}5d^1 Ln(II) ions, we may instead target molecular designs where the electronic structure and physicochemical properties are more sensitive to changes in the coordination environment. Arene ligands provide a promising route towards these goals due to their ability to act as symmetry-allowed donors into vacant d-orbitals, and further stabilise lower oxidation states through back donation.[25–32] Indeed, the only examples of formally zero-valent rare earth complexes are within [M(η^6-C$_6$R$_6$)$_2$] frameworks.[33–37]

[a]*Centre for Radiochemistry Research, The University of Manchester, Oxford Road, Manchester, M13 9PL, UK*

[b]*Department of Chemistry, The University of Manchester, Oxford Road, Manchester, M13 9PL, UK*

[c]*Research School of Chemistry, The Australian National University, Sullivans Creek Road, Canberra, 2601, Australia*

[d]*Photon Science Institute, The University of Manchester, Oxford Road, Manchester, M13 9PL, UK*

† Electronic supplementary information (ESI) available: Details of the starting materials used, descriptions of sample preparation for spectroscopic measurements, and methodologies and coordinates for the DFT and CASSCF calculations. CCDC 2266235, 2266236, 2266243, 2266244, 2266255–2266258, 2266261–2266264, 2282041, 2295306 and 2295307. For ESI and crystallographic data in CIF or other electronic format see DOI: https://doi.org/10.1039/d4sc03005b.

Herein, we present a series of structurally analogous bis-tethered arene divalent rare earth complexes of the form $[M(NHAr^{iPr_6})_2]$ (**2M**, M = Sc, Y, La, Sm, Eu, Tm, Yb; $NHAr^{iPr_6}$ = {N(H)C_6H_3-2,6-(C_6H_2-2,4,6-iPr_3)$_2$}) – the synthesis and some properties of **2Y** have been reported previously.[38] In all cases, characterisation using SQUID magnetometry, solid and solution phase EPR spectroscopy, UV-Vis-NIR spectroscopy, density functional theory (DFT), and complete active space self-consistent field (CASSCF) calculations support the description of these as formal Ln(II) complexes, demonstrating that this framework is robust across a range of Ln(II) ion sizes and (formal) reduction potentials. While all seven divalent complexes display close metal–arene contacts, only **2Sc**, **2Y**, and **2La** show mixing of a metal valence $nd_{(x^2-y^2)}$ orbital with the arene π* to give δ-bonding interactions. Complexes **2Sm**, **2Eu**, **2Tm**, and **2Yb** instead adopt metal-localised $4f^{n+1}$ configurations in accordance with their large Ln(II) $4f^{n+1} \rightarrow 4f^n5d^1$ promotional energies.[39,40] Solid and solution phase UV-Vis-NIR and EPR for **2Y**, combined with DFT calculations, reveals that the balance of metal *vs.* arene-centred spin-density is sensitive to small structural changes between these phases, suggesting the properties of divalent rare earth complexes with nd^1 may be tuned through ligand design.

Results and discussion

Synthesis

A reductive route was pursued for the synthesis of **2M** (M = Sc, Y, La, and Tm; Scheme 1A), which began with the synthesis of trivalent $[M(NHAr^{iPr_6})_2(I)]$ (**1M**, M = Sc, Y, La, Tm) precursors. Complexes **1M** were synthesised by salt elimination between $KNHAr^{iPr_6}$ (ref. 41 and 42) and the relevant rare earth tri-iodide salt $[MI_3(THF)_n]$ (n = 4, M = La; n = 3.5, M = Y, Tm; n = 3, M = Sc) in Et_2O.[43] Workup and crystallisation from toluene gave fair to good crystalline yields (47–62%). ^{1}H NMR spectroscopy of diamagnetic **1Sc**, **1Y**, and **1La** in d_6-benzene show the M···$C_{6\text{-arene}}$ interaction is dynamic in solution and that all four Tripp groups are in exchange (see ESI† for detailed assignments).[38]

Reduction (KC_8, 1.2 equiv.) of **1M** (M = Sc, Y, La, Tm) in Et_2O gave, after workup and crystallization from Et_2O, dark crystals of **2M** in fair crystalline yields (shown as % yield ahead): **2Sc** (red, 53%), **2Y** (red/green, 55%), **2La** (red/brown, 45%), and **2Tm** (red/brown, 65%). Salt elimination between $KNHAr^{iPr_6}$ and $MI_2(THF)_2$ (M = Sm, Eu, Yb)[44] in Et_2O gave poor to excellent isolated crystalline yields of **2Sm** (69%), **2Eu** (20%), and **2Yb** (82%) (Scheme 1B). Attempts to synthesise **1Sm** and **1Yb** using $[MI_3(THF)_n]$ precursors were unsuccessful, leading to intractable mixtures (see ESI†), and we did not attempt the synthesis of **1Eu**.

While the ^{1}H NMR spectra of **1Sc**, **1Y**, and **1La** showed the metal-bound and "terminal" {C_6H_2-2,4,6-iPr_3} (Tripp) groups were in exchange at room temperature, the spectrum of diamagnetic **2Yb** in d_6-benzene shows six doublets for the CH_3-*i*Pr groups, along with a single N(H) resonance. Thus, **2Yb** is C_2 symmetric in solution and the Tripp groups do not appreciably exchange at room temperature. This does not appear to be due to steric hindrance as the Sc(III) in **1Sc** is smaller than Yb(II) (6-coordinate radii: Yb(II), 0.868 Å; Sc(III), 0.745 Å). A variable temperature ^{1}H NMR study in d_8-toluene shows the CH_3-*i*Pr peaks begin to coalesce at 308 K, but full equilibrium is not reached until *ca.* 358 K (Fig. S40 and S41†). The ^{171}Yb–^{1}H HMBC NMR spectrum gave two cross-peaks at $\delta_{^{171}Yb} = -83$ ppm ($\delta_{^1H}$ = 3.53 and 7.02 ppm), showing the ^{171}Yb couples to both the anilido proton and the Tripp 3,5-CH groups. The ^{1}H NMR spectra of paramagnetic **2M** complexes were uninformative, see the ESI† for all NMR spectra.

Molecular structures

Single crystal X-ray diffraction studies on **1M** (M = Sc, Y, La, Tm) show all crystallize in the triclinic space group $P\bar{1}$ (Z' = 1) and are pseudo three-coordinate – see Fig. 1. In **1La**, the metal is sandwiched almost equally between two Tripp groups (La···$C_{6\text{-centroid}}$ = 2.8714(12) and 2.8783(12) Å; La···N_2I plane deviation = 0.0042(15) Å). Conversely, **1Sc** and **1Y** have a single Tripp group close to the metal (M···$C_{6\text{-centroid}}$: **1Sc**, 2.3391(8) Å; and **1Y**, 2.4949(9) Å) and hence are trigonal pyramidal. The structure of **1Y** is comparable to recently reported $[Y(NHAr^{iPr_6})_2(Cl)]$.[38] See the ESI† for the structure of **1Tm**, and a comparison of **1M** complexes. In the following sections, we shall continue to use the term "$C_{6\text{-centroid}}$", noting it is not strictly appropriate to define a centroid for non-planar groups.

The molecular structures of **2Sc**, **2Y**, and **2La** are also shown in Fig. 1 (see ESI† for **2Sm**, **2Eu**, **2Tm**, and **2Yb**). With the exception of **2Sc**, all **2M** complexes (M = Y, La, Sm, Eu, Tm, Yb) show two Tripp groups closely approaching the metal. When viewed along the $C_{6\text{-centroid}}$···$C_{6\text{-centroid}}$ axis these groups are either fully eclipsed due to crystallographic C_2 symmetry (**2Y**, **2Eu**, and **2Yb**), or are pseudo-eclipsed (**2Sc**, **2La**, **2Sm**, and **2Tm**). In **2Sc**, only one Tripp group is close to the metal. The nature of this metal–arene interaction provides insight into the electronic structure *vis-à-vis* metal- or ligand-centred

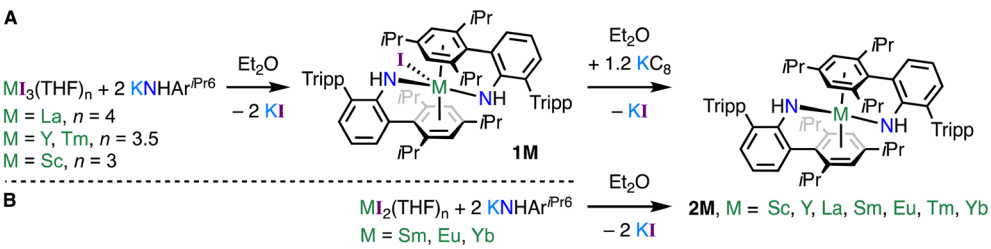

Scheme 1 Synthesis of (Route A) $[M(NHAr^{iPr_6})_2(I)]$ (**1M**, M = Sc, Y, La, Tm), and (Route B) $[M(NHAr^{iPr_6})_2]$ (M = Sc, Y, La, Sm, Eu, Tm, Yb). Tripp = {C_6H_2-2,4,6-iPr_3}.

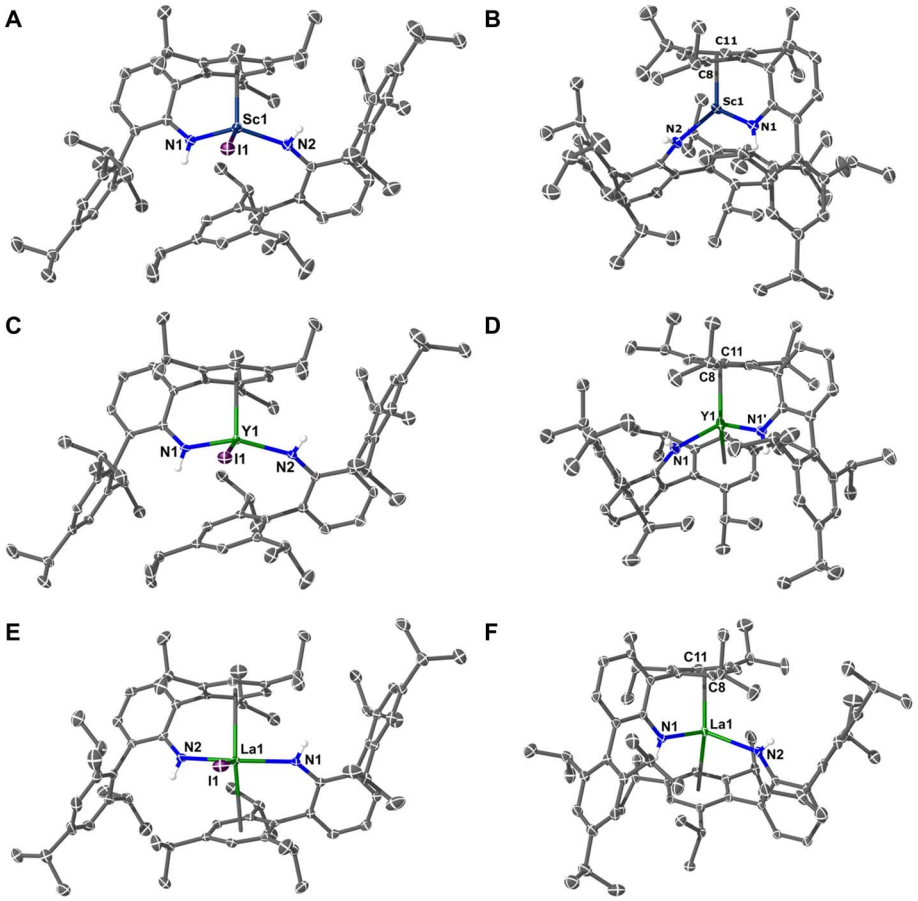

Fig. 1 Molecular structures: (A) **1Sc**; (B) **2Sc**; (C) **1Y**; (D) **2Y**; (E) **1La**; (F) **2La**. Thermal ellipsoids have been set at 40% probability. H-atoms except those on N–H groups, solvents of crystallization, and disordered components have been removed for clarity.

reduction.[45,46] Complexes **2Sc** and **2La** crystallize with a whole molecule in the asymmetric unit, and in both one metal-bound Tripp group is non-planar, showing an "open book" deformation for which a "hinge angle" ($\angle_{arene}$) can be calculated – 11.43(11)° for **2Sc**, and 12.9(3)° for **2La**. In **2Sc**, the next shortest M···$C_{6\text{-centroid}}$ distance (3.8304(7) Å) is too long to constitute a strong interaction; but, in **2La** the equivalent group is only *ca.* 0.4 Å further (M···$C_{6\text{-centroid}}$ = 2.8348(12) Å) than the deformed arene ring, but is planar. Complex **2Sc** is similar to the Ti(IV) analogue **2Ti**,[46] but the latter exhibits $\angle_{arene}$ of 24.19(18)° and is diamagnetic by SQUID magnetometry, indicating the presence of a dianionic Tripp ring.

Complex **2Y** is different to **2Sc** and **2La** as only half the molecule is present in the asymmetric unit ($Z' = 0.5$), as previously reported;[38] and also to that of **2U**.[47] The $\angle_{arene}$ angle for both ligands in **2Y** is 7.27(12)°, which compares well to 9.5(1)° in **2U**.[47] There is no clear trend in $\angle_{arene}$ values (**2Y** < **2U** < **2La** < **2Sc**) except that C_2 symmetric complexes (**2Y** and **2U**) have smaller $\angle_{arene}$ angles,[38,47] and that larger values (with a single deformed arene) correlate with a greater degree of metal electron localisation (see below). The Gd(0) complex, [Gd(C_6H_3-1,3,5-*t*Bu)$_2$], also displays two symmetry-equivalent distorted arene rings ($\angle_{arene}$ = 3.1(3)°).[33] The remaining divalent complexes, **2Sm**, **2Eu**, **2Tm**, and **2Yb**, are analogous to **2La**, except only the latter shows arene deformation. Table 1 summarizes all **2M** complexes now reported (M = Sc, Y, La, Sm, Eu, Tm, Yb, U).[38,47]

UV-Vis-NIR spectroscopy

UV-Vis-NIR spectra were collected for **1M** (M = Sc, Y, La, Tm) and **2M** (M = Sc, Y, La, Sm, Eu, Tm, Yb) at ambient temperature as 1 mM solutions in Et_2O (Fig. 2, except for **1Tm**). The spectra of **1Sc**, **1Y**, and **1La** are uninformative, showing only a broad ligand-to-metal charge transfer (LMCT) process from *ca.* 20 000 cm^{-1} (500 nm) to well into the UV region, accounting for the intense yellow colour of all three in solution. The colours and spectra of **1Tm** and **2Sm**, **2Eu**, **2Tm**, and **2Yb** are typical for these elements in their respective oxidation states (see ESI†).[13,14,48–51]

The spectrum of **2Sc** shows three well-resolved absorptions at 13 400 cm^{-1} (756 nm, 805 M^{-1} cm^{-1}), 17 400 cm^{-1} (575 nm, 1727 M^{-1} cm^{-1}), and 21 300 cm^{-1} (469 nm, 2471 M^{-1} cm^{-1}). The modest intensity of these peaks coupled with their energies suggests 3d → 3d transitions and/or metal-to-ligand charge transfer (MLCT) bands. For **2Y**, two peaks are resolved at 13 700 cm^{-1} (729 nm, 594 M^{-1} cm^{-1}) and 21 600 cm^{-1} (463 nm, 1787 M^{-1} cm^{-1}), while a third tails in from above 26 000 cm^{-1} (385 nm), in agreement with the previous report.[38] Finally, in **2La**, a single clear peak is resolved at 12 300 cm^{-1} (816 nm,

Table 1 Bond lengths (Å) and angles (°) for [M(NHAr^{iPr6})$_2$] (**2M**, M = Sc, Y, La, Sm, Eu, Tm, Yb, U)[38,47]

(Å or °)		**2Sc**	**2Y**[a]	**2La**	**2Sm**	**2Eu**[b]	**2Tm**	**2Yb**[b]	**2U**
M–N	N(1)	2.0884(11)	2.2600(12)	2.395(3)	2.412(2)	2.411(4) 2.414(5)[b]	2.3060(17)	2.310(6) 2.294(6)[b]	2.330(2)
	N(2)	2.0678(10)	—[a]	2.434(3)	2.425(2)	—[b]	2.3169(18)	—[b]	—[a]
M–C$_{6\text{-range}}$	Ring(1)	2.3913(12)–2.6304(14)	2.7276(14)–2.9273(15)	2.778(16)–2.971(9)	2.955(3)–3.160(3)	2.972(4)–3.176(5)	2.8015(19)–2.971(2)	2.840(6)–3.047(6)	2.723(3)–2.870(3)
	Ring(2)	—	—[a]	3.047(3)–3.240(3)	2.953(3)–3.201(3)	—[b]	2.819(2)–3.118(2)	—[b]	—[a]
M–C	C(8)	2.3913(12)	2.7684(14)	2.843(13)	—	—	—	—	2.731(3)
	C(11)	2.5418(13)	2.7859(15)	2.903(12)	—	—	—	—	2.723(3)
Arene fold angle		11.43(11)	7.27(12)	12.9(9)	—	—	—	—	9.3(2)

[a] The solid-state structure is C_2-symmetric so there is a single metal and ligand per asymmetric unit. [b] The solid-state structures show two half-molecules in the asymmetric unit, so M(1) and M(2) each have only one unique ligand.

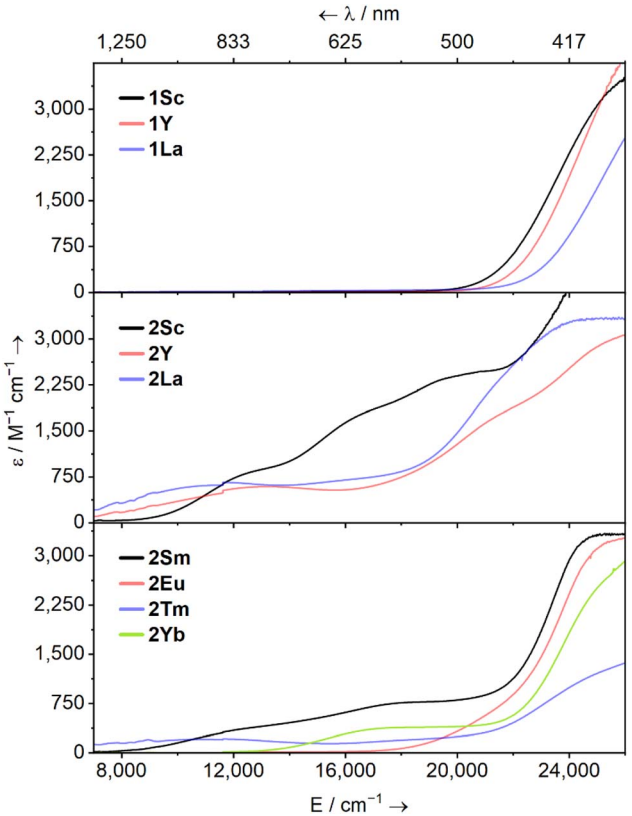

Fig. 2 Solution UV-Vis-NIR spectra of [M(NHAr^{iPr6})(I)] (**1M**, M = Sc, Y, La; top) and [M(NHAr^{iPr6})] (**2M**, middle, M = Sc, Y, La; bottom, M = Sm, Eu, Tm, Yb) – as 1 mM solutions in Et$_2$O between 7000–26 000 cm^{-1} (1429–385 nm) at ambient temperature.

650 M^{-1} cm^{-1}), which we suggest is a 5d → 5d transition. A broad feature at *ca.* 16 000 cm^{-1} and a peak with a maximum at *ca.* 24 000 cm^{-1} (417 nm) can also be seen, but background absorption precludes accurately describing these.

SQUID magnetometry

Direct current (DC) magnetic susceptibility data were collected for **1Tm**, and **2M** (M = Sc, Y, La, Sm, Eu, Tm) from 1.8 to 300 K under an applied field of 1 kOe. At 300 K, the $\chi_M T$ (χ_M is the molar magnetic susceptibility) values for **1Tm** (6.61 cm^3 mol^{-1} K), **2Eu** (7.27 cm^3 mol^{-1} K), and **2Tm** (2.47 cm^3 mol^{-1} K) closely match theoretical values for 4f^{n+1} configurations for Tm(III), 4f^{12} (^{3}H$_6$, 7.15 cm^3 mol^{-1} K), Eu(II), 4f^7 (^{8}S$_{7/2}$, 7.88 cm^3 mol^{-1} K), and Tm(II), 4f^{13} (^{2}F$_{7/2}$, 2.57 cm^3 mol^{-1} K). For **2Sm** (4f^6) the value at 300 K is 1.43 cm^3 mol^{-1} K, which is in the range observed for Eu(III) (4f^6) complexes (1.3 to 1.5 cm^3 mol^{-1} K),[52] and is non-zero due to population of excited ^{7}F$_J$ states.[48–50] Upon cooling to 1.8 K, $\chi_M T$ for **2Sm** lowers to 0.02 cm^3 mol^{-1} K which is consistent with a ^{7}F$_0$ ground state; thus, a 4f^6 configuration.

Complexes **2Sc**, **2Y** and **2La** exhibit $\chi_M T$ values at 300 K (0.31, 0.36, and 0.29 cm^3 mol^{-1} K respectively), which are in reasonable agreement with the spin-only value for an $S = 1/2$ system (0.375 cm^3 mol^{-1} K for $g = 2.00$), and hence with a formal d^1 configuration. In each case, the magnetic moment is essentially invariant with temperature down to 8–10 K, where a sudden

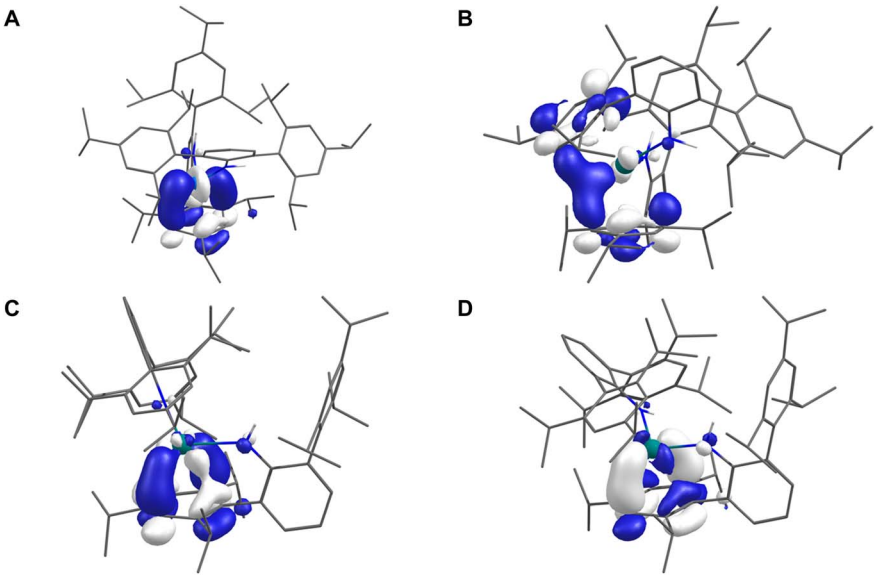

Fig. 3 SOMOs of: (A) **2Sc**; (B) **2Y**; (C) **2La**; (D) **2Y-Et$_2$O** (isovalues = 0.05) using geometries derived from single crystal X-ray diffraction with H-atoms optimised (**2Sc**, **2Y**), select disordered C-atoms and all H-atoms optimised (**2La**), or all atom positions optimised (**2Y-Et$_2$O**). H-atoms except those of the N(H) group omitted for clarity.

drop can be seen, though this varies across independently synthesised samples (see ESI† for more details).

Electronic structure calculations

Unrestricted Kohn–Sham density-functional theory (DFT) calculations were performed on **2Sc**, **2Y**, **2La**, **2Tm** ($S = 1/2$), **2Sm** ($S = 3$), **2Eu** ($S = 7/2$), and **2Yb** ($S = 0$) using partially geometry-optimised structures (see ESI† for full details). Löwdin population and spin analyses of **2Sm**, **2Eu**, **2Yb**, and **2Tm** are consistent with experimental data and describe all four as $4f^{n+1}$ Ln(II) ions with metal-localised valence electrons. Fig. 3A and C shows the SOMOs of **2Sc** and **2La**, which depict M–arene δ-bonds comprised of 36% 3d (with 4% 4s) and 14% 5d (with 10% 4f and 1% 6s) metal character, respectively, with the bound Tripp ring making up 41% (**2Sc**) and 56% (**2La**) – the remainder is diffused over the rest of the molecule. Defining the M···Tripp direction as z, the d-orbital contribution is described as $d_{(xy/x^2-y^2)}$ (the superficial resemblance to d_{x^2} or d_{y^2} is due to a small degree of d_{z^2} mixing in this axis system) – this is comparable to the e_{2g} MO of bis-benzene transition metal complexes in D_{6h} symmetry.[53]

In the case of **2Y** (Fig. 3B), the SOMO is delocalised across the symmetry equivalent metal-bound Tripp groups such that the SOMO composition is 14% Y (12% 4d, 0.5% 5s), while the bound Tripp rings sum to 64.6% – the SOMO resembles a delocalised δ-bonding interaction. These results agree with previous work on **2Y**,[38] but it is an outlier compared to **2Sc** and **2La**. Full geometry optimisation of **2Y** using the lower-symmetry structure of **2La** as the starting point was performed in the gas phase and using an Et_2O solvent model (**2Y-Et$_2$O** henceforth). Both calculations produced geometries that have only one metal-bound Tripp group deformed (*i.e.* like **2Sc** and **2La**) and are true local minima on the potential energy surface. Fig. 3D shows the SOMO of **2Y-Et$_2$O**, and Löwdin population analysis shows it to be more metal-localised (22% 4d, 2% 5s, and 1% 4f – total 25%) than in the C_2-symmetric **2Y** (14%), which is accompanied by a corresponding decrease in Tripp

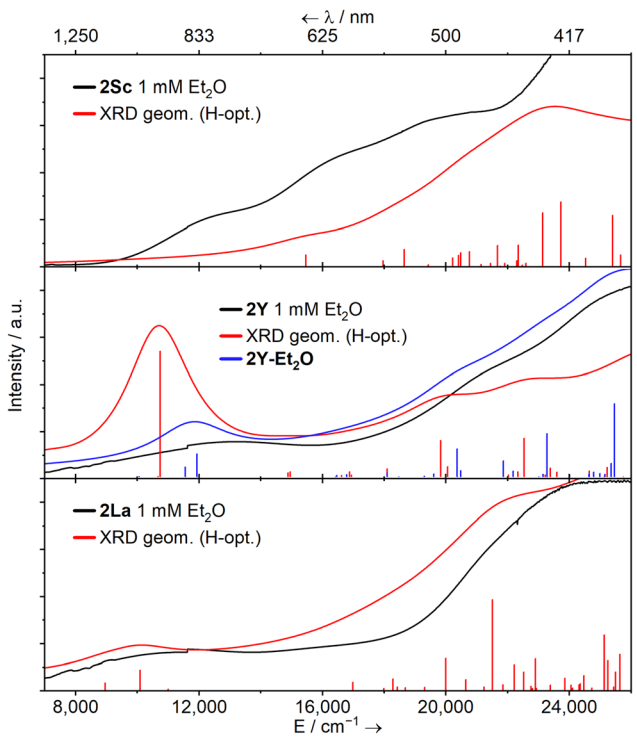

Fig. 4 Experimental (1 mM, Et_2O, black), calculated sTD-DFT transitions (red and blue vertical lines), and simulated spectra (red and blue solid lines, with Gaussian broadening and a linewidth factor of $25 \times \sqrt{E}$) UV-Vis-NIR spectra for complexes **2Sc**, **2Y** (and **2Y-Et$_2$O**) and **2La** calculated transitions were performed using a solvent model accounting for the dielectric constant (ε) and refractive index (n_D) of Et_2O.

contributions to the SOMO – 65% in **2Y** (over two Tripp groups) and 56% in **2Y-Et$_2$O** (over a single Tripp group). The Löwdin spin populations at the metal in **2Y-Et$_2$O** (0.245) and **2Y** (0.142) reflect these differences.

Time-dependent DFT (TD-DFT) and simplified TD-DFT (sTD-DFT) calculations were employed to model the UV-Vis-NIR spectra of **2Sc**, **2Y**, **2La**, and **2Y-Et$_2$O**; here we focus on sTD-DFT with TPSSh for consistency with prior art (Fig. 4),[11,12,16,23,54–56] see ESI (Fig. S102–S111†) for more details. Experimental features of **2Sc** and **2La** are well represented, and the Natural Transition Orbitals (NTOs) suggests the broad features in the spectrum of **2Sc** are 3d → 3d transitions, the lowest energy of which resembles a $3d_{(xy/x^2-y^2)} \rightarrow 3d_{(x^2-y^2/xy)}$ transition maintaining the δ-bonding interaction. For **2La**, the lowest energy feature is a $5d_{(xy/x^2-y^2)} \rightarrow 5d_{(x^2-y^2/xy)}$ transition, and the next two lowest energy features are a combination of MLCT and 5d → 5d transitions. There is poor agreement with all methods for **2Y** (Fig. 4 middle panel, red line), however, calculations for **2Y-Et$_2$O** are substantially better (Fig. 4 middle panel, blue line); this suggests that the structure of **2Y** in Et$_2$O solution is similar to the solid-state structures of **2Sc** and **2La**. The lowest energy feature in **2Y-Et$_2$O** is comprised of two components, a $4d_{(xy/x^2-y^2)} \rightarrow 4d_{(x^2-y^2/xy)}$ transition and an MLCT process.

Complete active space self-consistent field (CASSCF) calculations (see ESI†) on **2M** confirm the DFT and experimental results: **2Sc**, **2Y** and **2La** exhibit nd^1 ground states with significant orbital mixing with the arene ligand(s), and **2Sm**, **2Eu**, **2Tm** and **2Yb** have $4f^{n+1}$ ground states. Calculations for the lowest-lying excitations in **2Sc**, **2Y** and **2La** including multi-configurational pair-density functional theory (MC-PDFT) corrections for dynamic correlation show nd/arene → nd/arene excitations in the UV-Vis-NIR range, in good agreement with the experimental spectra. The character of these excitations is broadly in line with that found using (s)TD-DFT, where the lowest-lying excitations for **2Sc** are mostly localised to one side of the molecule and resemble d → d transitions, while some for **2La** and **2Y-Et$_2$O** are combined MLCT and 5d → 5d transitions to the opposite Tripp ring.

EPR spectroscopy

Continuous wave (c. w.) EPR spectroscopy was used to study the orbitally non-degenerate species **2Sc**, **2Y** and **2La**. All three are EPR active as polycrystalline solids and in solution (1 mM Et$_2$O or nPr$_2$O); spectra of **2Y** in Et$_2$O have been reported previously.[38] We find better resolved frozen solution spectra in nPr$_2$O than in Et$_2$O (although the spectra are consistent; see ESI†).

X-band spectra of powders at room temperature show features around $g = 2$, consistent with the formal M(II) oxidation states. There is partial resolution of the metal hyperfine for **2Sc** (^{45}Sc, $I = 7/2$, 100% abundant) and **2Y** (^{89}Y, $I = 1/2$, 100%) but is unresolved for **2La** (^{139}La, $I = 7/2$, 100%). For **2Sc**, a hyperfine octet is observed, with $g = 2.000$ and $A = 145$ MHz, for **2Y** we observe a hyperfine doublet (estimated $A = 14$ MHz) with $g_\perp = 2.005$ and $g_\parallel = 1.995$, and for **2La**, we observe $g_\perp = 2.019$ and $g_\parallel = 1.958$. There are small changes in these parameters upon cooling to 5 K, without any improvement in resolution; the limited resolution of the powder spectra is indicative of intermolecular magnetic interactions.

Fluid solution spectra of **2Y** and **2La** (Fig. 5 and Table 2) give a hyperfine doublet ($A_{iso} = 46$ MHz, $g_{iso} = 1.9995$) and octet ($A_{iso} = 112$ MHz, $g_{iso} = 1.998$), respectively. For **2Sc** (Fig. 5 and Table 2) we also obtain an octet ($A_{iso} = 205$ MHz, $g_{iso} = 1.989$), but there is a second minor octet spectrum which differs subtly in the magnitude of the hyperfine ($A_{iso} = 186$ MHz), suggesting

Table 2 Experimental (frozen solution) and calculated EPR parameters for **2Sc**, **2Y** and **2La**. Calculated hyperfine coupling constants in MHz; experimental A_{iso} calculated as $(A_\parallel + 2A_\perp)/3$. The calculated g_1/A_1 axes are along the M-bound arene direction

		g_1	g_2	g_3	A_1	A_2	A_3	A_{iso}
2Sc	Exp.	1.990	2.002		195	210		205
	Calc.	1.990	2.009	2.015	159	171	184	171
2Y	Exp.	1.986	2.004		−36	−39		−38
2Y-Et$_2$O	Calc.	1.983	2.004	2.006	−47	−49	−50	−48
2La	Exp.	1.952	2.005		100	110		107
	Calc.	1.954	1.971	1.993	101	106	108	105

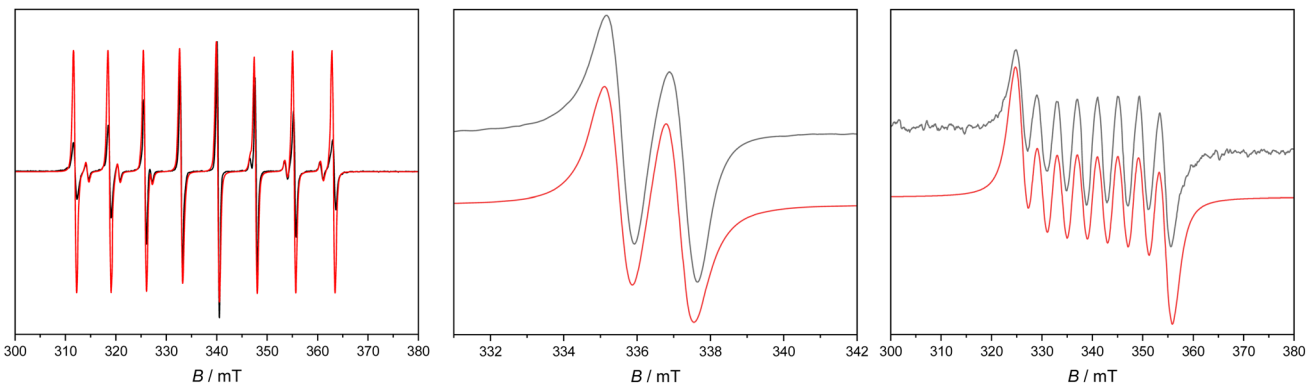

Fig. 5 X-band c. w. EPR spectrum of 1 mM **2Sc** in Et$_2$O at 250 K (left), **2Y** in nPr$_2$O at 180 K (middle), and **2La** in Et$_2$O at 200 K (right). Black, experimental; red, simulations with parameters in the text.

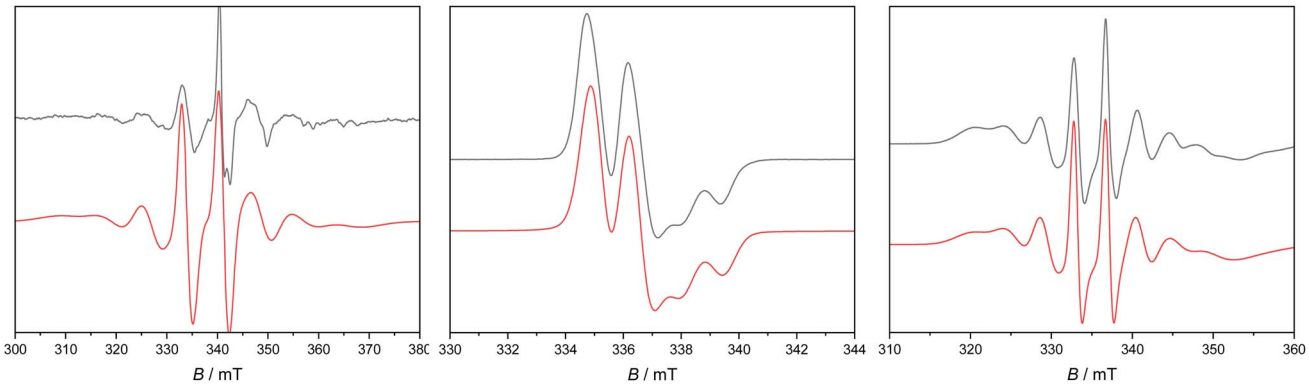

Fig. 6 X-band c. w. EPR spectrum of 1 mM **2Sc** (left) in Et_2O at 130 K, **2Y** (middle) and **2La** (right) in nPr_2O at 60 K. Black experimental, red simulations.

two Sc(II) species in solution with a relative abundance of *ca.* 12 : 1 (similar features have been observed recently in a different Sc(II) system[23]). In each case $g_{iso} < g_e$, consistent with the formal d^1 configuration. The isotropic part of the hyperfine interaction derives from s-orbital spin density, and from theoretical values of the hyperfine interaction for unit population of the valence s-orbitals[57] we estimate 7.3% (**2Sc**), 3.7% (**2Y**) and 2.0% (**2La**) s-orbital character of the SOMO; these are in good agreement with DFT calculations (3.6%, 1.8%, and 1.0% s-orbital character, or 3.8%, 2.0%, 1.1% Löwdin s-orbital spin populations). In summary, **2Sc** has the largest metal valence s-orbital spin density, then **2Y** > **2La**.

Frozen solutions gave well-resolved spectra in each case (Fig. 6 and Table 2). For **2Sc** there is a dominant perpendicular hyperfine coupling $A_\perp \approx 210$ MHz ($g_\perp = 2.002$), from which we can determine $A_\parallel \approx 195$ MHz (using $A_{iso} = 205$ MHz from the fluid spectra), and by simulation we find $g_\parallel = 1.99$. However, these parameters are not well defined as there is evidence of a second species. For **2Y** and **2La** the spectra appear axially symmetric giving $g_\perp = 2.004$, $g_\parallel = 1.986$, with a near isotropic metal hyperfine of $A_\perp = -39$, $A_\parallel = -36$ MHz for **2Y**, while for **2La** we find $g_\perp = 2.005$, $g_\parallel = 1.952$ with $A_\perp = 110$, $A_\parallel = 100$ MHz.

The anisotropy of the *g*-values for **2Sc**, **2Y** and **2La** is due to the significant d-orbital character of the SOMO. The $g_\perp > g_\parallel$ pattern indicates a dominant $d_{x^2-y^2}$ contribution (where *z* is the M-bound arene direction), while the greater deviation of $g_\parallel$ from g_e in the series **2La** > **2Y** > **2Sc** is in keeping with greater spin–orbit coupling for the heavier elements,[58] and also the trend in the lowest energy excited states (see above). A simple analysis of the anisotropic metal hyperfine interaction to give the metal $d_{x^2-y^2}$ contribution to the SOMO [$A_\parallel - A_\perp = (-6/7)a^2P_d$, where *a* is the $d_{x^2-y^2}$ coefficient of the SOMO and values of P_d are tabulated in ref. 57] gives 7.3% for **2Sc**, 5.6% for **2Y** and 4.9% for **2La**. DFT calculations give much larger d-orbital contributions of 36%, 20%, and 14%, respectively (see above), despite also showing reasonable agreement with the measured hyperfine coupling constants (Table 2), implying an inadequacy in the simple analysis above; we have previously noted similar discrepancies in related $[M^{II}L_3]^-$ systems (M = Sc, Y, La, Lu).[17]

Indeed, the EPR parameters and electronic structures of **2Sc**, **2Y** and **2La** contrast to those related d^1 $[M^{II}L_3]^-$ species where the trigonal crystal field instead stabilises the d_{z^2} (defined by the C_3 axis) orbital, or a d/s hybrid giving rise to characteristic $g_\perp < g_\parallel$ ($\approx g_e$) patterns.[2,16,17] The electronic structures of the present compounds have more in common with $[Sc(Cp^{ttt})_2]$,[23] where DFT calculations give a $d_{x^2-y^2}$-dominated SOMO, and a similar $g_\perp > g_\parallel$ pattern can be observed from the frozen solution EPR data. The hyperfine coupling in **2Y** and **2La** is much weaker than in the trigonal M(II) cyclopentadienyl species: for example, $[Y(Cp^R)_3]^-$ with various substituents [*e.g.* $(Cp^R)_3 = Cp'_3$, Cp^t_3, $\{Cp''_2(C_5H_5)\}$] have $|A_{iso}|$ = 98–130 MHz;[17,59,60] and $[La(Cp^R)_3]^-$ (Cp^R = Cp′, Cp″, Cp^{tt}) have $|A_{iso}|$ = 390–640 MHz.[2,17,61] Hence, there is greater metal character in the SOMOs of $[M(Cp^R)_3]^-$ than in **2M**. Comparing the present compounds with more symmetric sandwich compounds, $[Y(Cp^{iPr_5})_2]$ and $[La(Cp^{iPr_5})_2]$ have larger magnitude $|A_{iso}| = 505$ and 2000 MHz, respectively,[14] while curiously $[Sc(Cp^{ttt})_2]$ has smaller magnitude $|A_{iso}| = 83$ MHz,[23] although it has been reported that $[Sc(Cp^*)_2]$ (not structurally authenticated) has $|A_{iso}| = 824$ MHz.[23]

Conclusions

In summary, we have reported a series of room-temperature stable crystalline divalent rare earth bis-tethered arene complexes of the form $[M(NHAr^{iPr_6})_2]$ (**2M**; M = Sc, Y, La, Sm, Eu, Tm, Yb). In the case of Sc and La, these represent the second examples of neutral divalent complexes with these elements and are amongst just a few in any charge state. All **2M** complexes feature close metal–arene contacts, which in **2Sc**, **2Y**, and **2La**, results in an "open book" arene deformation suggestive of charge transfer, whereas in **2Sm**, **2Eu**, **2Tm**, and **2Yb** the equivalent arene groups remain planar. SQUID magnetometry and UV-Vis-NIR spectroscopy demonstrate **2Sm**, **2Eu**, **2Tm**, and **2Yb** are examples of $4f^{n+1}$ ions, and quantum chemical calculations show that the metal-localised 4f orbitals do not interact with the arene π-orbitals.

Solution-phase c. w. EPR spectroscopy of **2Sc**, **2Y**, and **2La** are consistent with formal nd^1 ions, where the SOMO has $nd_{(x^2-y^2)}$

character with delocalisation of the spin onto the Tripp groups. Quantum chemical and *ab initio* calculations further support this description and reveal mixing between metal $nd_{(x^2-y^2)}$ and arene–π orbitals to give δ-bonds, which explain the arene deformation in their structures.

The electronic structures of nd^1 **2Sc**, **2Y**, and **2La** closely resemble those of bis-benzene transition metal complexes; and, going forward, we posit that these rare $nd_{(x^2-y^2)}$ configurations afford as-yet unexplored opportunities to tune the physicochemical properties of divalent rare earth ions with formal $\{5d/6s\}^1$ valence electron configurations. This, along with work to probe the limits of the bis-$\{NHAr^{iPr_6}\}$ framework to stabilise other divalent f-block ions, remains an active area of research in our laboratory.

Data availability

The following CCDC references contain the ESI† crystal data for this article: **1Sc** (2266263), **1Y** (2266261), **1La** (2266235), **1Tm** (2266255), **1Yb** (2266257), $\mathbf{1Y^{\beta}}$ (2295306), $\mathbf{1La^{\beta}}$ (2295307), **2Sc** (2266264), **2Y** (2266262), **2La** (2266236), **2Sm** (2266243), **2Eu** (2266244), **2Tm** (2266256), **2Yb** (2266258), and **3** (2282041). Raw experimental data (NMR, ATR-IR, UV-Vis-NIR, SQUID Magnetometry) and computational inputs/outputs can be found freely at DOI: **https://doi.org/10.48420/25245760**.

Author contributions

C. A. P. G. provided the original concept. R. E. M. synthesised and characterised the complexes. R. E. M. and C. A. P. G. collected, solved, and refined the single crystal XRD data. G. F. S. W. performed final refinement and validation of XRD data. J. A. S. performed SQUID magnetometry measurements and interpreted the data. T. H. performed EPR spectroscopy measurements, E. J. L. M. and D. C. supervised the EPR measurements and data interpretation. C. A. P. G. performed DFT calculations and interpretation, N. F. C. performed CASSCF and MC-PDFT calculations and interpreted the data. C. A. P. G. wrote the manuscript with contributions from all other authors.

Conflicts of interest

There are no conflicts to declare.

Acknowledgements

We thank the Royal Society for a University Research Fellowship (URF\211271 to C. A. P. G., and URF\191320 to N. F. C.); and the UoM Department of Chemistry for the funding of a PhD studentship under EPSRC DTP (EP/W524347/1 to R. E. M., and EP/T517823/1 to T. H.). We acknowledge funding from the EPSRC (EP/K039547/1, EP/V007580/1, and EP/P001386/1 for NMR spectroscopy and X-ray diffraction). We also thank the EPSRC UK EPR National Research Facility including for access to the SQUID magnetometer (EP/W014521/1, EP/V035231/1, EPS033181/1). C. A. P. G. and N. F. C. also thank the Computational Shared Facility at the University of Manchester for support. We thank Prof. Stephen Liddle for support (J. A. S.). Elemental analyses were performed at the UoM by Mr Martin Jennings and Ms Anne Davies. We are also grateful to Prof. Aaron Odom and Prof. Selvan Demir for scientific discussions and encouragement.

References

1 K. R. Meihaus, M. E. Fieser, J. F. Corbey, W. J. Evans and J. R. Long, *J. Am. Chem. Soc.*, 2015, **137**, 9855–9860.
2 J. Liu, L. E. Nodaraki, D. O. T. A. Martins, M. J. Giansiracusa, P. J. Cobb, J. Emerson-King, F. Ortu, G. F. S. Whitehead, G. K. Gransbury, E. J. L. Mclnnes, F. Tuna and D. P. Mills, *Eur. J. Inorg. Chem.*, 2023, **26**, e202300552.
3 M. R. MacDonald, J. W. Ziller and W. J. Evans, *J. Am. Chem. Soc.*, 2011, **133**, 15914–15917.
4 M. R. MacDonald, J. E. Bates, M. E. Fieser, J. W. Ziller, F. Furche and W. J. Evans, *J. Am. Chem. Soc.*, 2012, **134**, 8420–8423.
5 M. R. MacDonald, J. E. Bates, J. W. Ziller, F. Furche and W. J. Evans, *J. Am. Chem. Soc.*, 2013, **135**, 9857–9868.
6 M. E. Fieser, M. G. Ferrier, J. Su, E. Batista, S. K. Cary, J. W. Engle, W. J. Evans, J. S. Lezama Pacheco, S. A. Kozimor, A. C. Olson, A. J. Ryan, B. W. Stein, G. L. Wagner, D. H. Woen, T. Vitova and P. Yang, *Chem. Sci.*, 2017, **8**, 6076–6091.
7 M. T. Trinh, J. C. Wedal and W. J. Evans, *Dalton Trans.*, 2021, **50**, 14384–14389.
8 T. F. Jenkins, D. H. Woen, L. N. Mohanam, J. W. Ziller, F. Furche and W. J. Evans, *Organometallics*, 2018, **37**, 3863–3873.
9 A. J. Ryan, L. E. Darago, S. G. Balasubramani, G. P. Chen, J. W. Ziller, F. Furche, J. R. Long and W. J. Evans, *Chem.–Eur. J.*, 2018, **24**, 7702–7709.
10 S. A. Moehring, M. Miehlich, C. J. Hoerger, K. Meyer, J. W. Ziller and W. J. Evans, *Inorg. Chem.*, 2020, **59**, 3207–3214.
11 D. N. Huh, S. R. Ciccone, S. Bekoe, S. Roy, J. W. Ziller, F. Furche and W. J. Evans, *Angew. Chem., Int. Ed.*, 2020, **59**, 16141–16146.
12 L. M. Anderson-Sanchez, J. M. Yu, J. W. Ziller, F. Furche and W. J. Evans, *Inorg. Chem.*, 2023, **62**, 706–714.
13 M. E. Fieser, M. R. MacDonald, B. T. Krull, J. E. Bates, J. W. Ziller, F. Furche and W. J. Evans, *J. Am. Chem. Soc.*, 2015, **137**, 369–382.
14 K. R. McClain, C. A. Gould, D. A. Marchiori, H. Kwon, T. T. Nguyen, K. E. Rosenkoetter, D. Kuzmina, F. Tuna, R. D. Britt, J. R. Long and B. G. Harvey, *J. Am. Chem. Soc.*, 2022, **144**, 22193–22201.
15 P. W. Smith, J. Hrubý, W. J. Evans, S. Hill and S. G. Minasian, *J. Am. Chem. Soc.*, 2024, **146**, 5781–5785.
16 K. Kundu, J. R. K. White, S. A. Moehring, J. M. Yu, J. W. Ziller, F. Furche, W. J. Evans and S. Hill, *Nat. Chem.*, 2022, **14**, 392–397.
17 A.-M. Ariciu, D. H. Woen, D. N. Huh, L. E. Nodaraki, A. K. Kostopoulos, C. A. P. Goodwin, N. F. Chilton,

E. J. L. McInnes, R. E. P. Winpenny, W. J. Evans and F. Tuna, *Nat. Commun.*, 2019, **10**, 3330.
18 C. A. Gould, K. R. McClain, J. M. Yu, T. J. Groshens, F. Furche, B. G. Harvey and J. R. Long, *J. Am. Chem. Soc.*, 2019, **141**, 12967–12973.
19 P.-B. Jin, Q.-C. Luo, G. K. Gransbury, I. J. Vitorica-Yrezabal, T. Hajdu, I. Strashnov, E. J. L. McInnes, R. E. P. Winpenny, N. F. Chilton, D. P. Mills and Y.-Z. Zheng, *J. Am. Chem. Soc.*, 2023, **145**, 27993–28009.
20 C. A. Gould, K. R. McClain, D. Reta, J. G. C. Kragskow, D. A. Marchiori, E. Lachman, E. S. Choi, J. G. Analytis, R. D. Britt, N. F. Chilton, B. G. Harvey and J. R. Long, *Science*, 2022, **375**, 198–202.
21 J. C. Wedal, L. M. Anderson-Sanchez, M. T. Dumas, C. A. Gould, M. J. Beltran-Leiva, C. Celis-Barros, D. Paez-Hernandez, J. W. Ziller, J. R. Long and W. J. Evans, *J. Am. Chem. Soc.*, 2023, **145**, 10730–10742.
22 K. R. McClain, H. Kwon, K. Chakarawet, R. Nabi, J. G. C. Kragskow, N. F. Chilton, R. D. Britt, J. R. Long and B. G. Harvey, *J. Am. Chem. Soc.*, 2023, **145**, 8996–9002.
23 J. D. Queen, L. M. Anderson-Sanchez, C. R. Stennett, A. Rajabi, J. W. Ziller, F. Furche and W. J. Evans, *J. Am. Chem. Soc.*, 2024, **146**, 3279–3292.
24 J. T. Boronski, J. A. Seed, D. Hunger, A. W. Woodward, J. van Slageren, A. J. Wooles, L. S. Natrajan, N. Kaltsoyannis and S. T. Liddle, *Nature*, 2021, **598**, 72–75.
25 M. D. Straub, E. T. Ouellette, M. A. Boreen, R. D. Britt, K. Chakarawet, I. Douair, C. A. Gould, L. Maron, I. Del Rosal, D. Villarreal, S. G. Minasian and J. Arnold, *J. Am. Chem. Soc.*, 2021, **143**, 19748–19760.
26 J. D. Cryer and S. T. Liddle, in *Comprehensive Organometallic Chemistry IV*, ed. G. Parkin, K. Meyer and D. O'Hare, Elsevier, Oxford, 2022, pp. 460–501.
27 J. Murillo, R. Bhowmick, K. L. M. Harriman, A. Gomez-Torres, J. Wright, R. W. Meulenberg, P. Miro, A. Metta-Magana, M. Murugesu, B. Vlaisavljevich and S. Fortier, *Chem. Sci.*, 2021, **12**, 13360–13372.
28 R. A. Keerthi Shivaraam, M. Keener, D. K. Modder, T. Rajeshkumar, I. Zivkovic, R. Scopelliti, L. Maron and M. Mazzanti, *Angew. Chem., Int. Ed.*, 2023, **62**, e202304051.
29 M. Keener, R. A. K. Shivaraam, T. Rajeshkumar, M. Tricoire, R. Scopelliti, I. Zivkovic, A. S. Chauvin, L. Maron and M. Mazzanti, *J. Am. Chem. Soc.*, 2023, **145**, 16271–16283.
30 F.-C. Hsueh, T. Rajeshkumar, L. Maron, R. Scopelliti, A. Sienkiewicz and M. Mazzanti, *Chem. Sci.*, 2023, **14**, 6011–6021.
31 Y. Wang, J. Liang, C. Deng, R. Sun, P.-X. Fu, B.-W. Wang, S. Gao and W. Huang, *J. Am. Chem. Soc.*, 2023, **145**, 22466–22474.
32 H. S. La Pierre, A. Scheurer, F. W. Heinemann, W. Hieringer and K. Meyer, *Angew. Chem., Int. Ed.*, 2014, **53**, 7158–71562.
33 J. G. Brennan, F. G. N. Cloke, A. A. Sameh and A. Zalkin, *J. Chem. Soc., Chem. Commun.*, 1987, 1668–1669.
34 D. M. Anderson, F. G. N. Cloke, P. A. Cox, N. Edelstein, J. C. Green, T. Pang, A. A. Sameh and G. Shalimoff, *J. Chem. Soc., Chem. Commun.*, 1989, 53–55.
35 W. A. King, T. J. Marks, D. M. Anderson, D. J. Duncalf and F. G. N. Cloke, *J. Am. Chem. Soc.*, 1992, **114**, 9221–9223.
36 F. G. N. Cloke, *Chem. Soc. Rev.*, 1993, **22**, 17–24.
37 W. A. King, S. Di Bella, G. Lanza, K. Khan, D. J. Duncalf, F. G. N. Cloke, I. L. Fragala and T. J. Marks, *J. Am. Chem. Soc.*, 1996, **118**, 627–635.
38 R. Jena, F. Benner, F. Delano, D. Holmes, J. McCracken, S. Demir and A. L. Odom, *Chem. Sci.*, 2023, **14**, 4257–4264.
39 P. Dorenbos, *J. Condens. Matter Phys.*, 2003, **15**, 575–594.
40 P. Dorenbos, *J. Lumin.*, 2000, **91**, 91–106.
41 B. R. Barnett, C. C. Mokhtarzadeh, P. Lummis, S. Wang, J. D. Queen, J. Gavenonis, N. Schüwer, T. D. Tilley, J. N. Boynton, N. Weidemann, D. W. Agnew, P. W. Smith, T. B. Ditri, A. E. Carpenter, J. K. Pratt, N. D. Mendelson, J. S. Figueroa and P. P. Power, in *Inorganic Syntheses*, 2018, pp. 85–122.
42 B. Twamley, C.-S. Hwang, N. J. Hardman and P. P. Power, *J. Organomet. Chem.*, 2000, **609**, 152–160.
43 K. Izod, S. T. Liddle and W. Clegg, *Inorg. Chem.*, 2004, **43**, 214–218.
44 P. Girard, J. L. Namy and H. B. Kagan, *J. Am. Chem. Soc.*, 1980, **102**, 2693–2698.
45 S. R. Chowdhury, C. A. P. Goodwin and B. Vlaisavljevich, *Chem. Sci.*, 2024, **15**, 1810–1819.
46 J. N. Boynton, J. D. Guo, F. Grandjean, J. C. Fettinger, S. Nagase, G. J. Long and P. P. Power, *Inorg. Chem.*, 2013, **52**, 14216–14223.
47 B. S. Billow, B. N. Livesay, C. C. Mokhtarzadeh, J. McCracken, M. P. Shores, J. M. Boncella and A. L. Odom, *J. Am. Chem. Soc.*, 2018, **140**, 17369–17373.
48 N. F. Chilton, C. A. P. Goodwin, D. P. Mills and R. E. P. Winpenny, *Chem. Commun.*, 2015, **51**, 101–103.
49 C. A. P. Goodwin, K. C. Joslin, S. J. Lockyer, A. Formanuik, G. A. Morris, F. Ortu, I. J. Vitorica-Yrezabal and D. P. Mills, *Organometallics*, 2015, **34**, 2314–2325.
50 C. A. P. Goodwin, N. F. Chilton, G. F. Vettese, E. Moreno Pineda, I. F. Crowe, J. W. Ziller, R. E. P. Winpenny, W. J. Evans and D. P. Mills, *Inorg. Chem.*, 2016, **55**, 10057–10067.
51 C. A. P. Goodwin, N. F. Chilton, L. S. Natrajan, M.-E. Boulon, J. W. Ziller, W. J. Evans and D. P. Mills, *Inorg. Chem.*, 2017, **56**, 5959–5970.
52 Y. Takikawa, S. Ebisu and S. Nagata, *J. Phys. Chem. Solids*, 2010, **71**, 1592–1598.
53 V. M. Rayón and G. Frenking, *Organometallics*, 2003, **22**, 3304–3308.
54 A. Rajabi, R. Grotjahn, D. Rappoport and F. Furche, *Dalton Trans.*, 2024, **53**, 410–417.
55 M. E. Fieser, C. T. Palumbo, H. S. La Pierre, D. P. Halter, V. K. Voora, J. W. Ziller, F. Furche, K. Meyer and W. J. Evans, *Chem. Sci.*, 2017, **8**, 7424–7433.
56 C. T. Palumbo, D. P. Halter, V. K. Voora, G. P. Chen, A. K. Chan, M. E. Fieser, J. W. Ziller, W. Hieringer, F. Furche, K. Meyer and W. J. Evans, *Inorg. Chem.*, 2018, **57**, 2823–2833.
57 J. R. Morton and K. F. Preston, *J. Magn. Reson.*, 1978, **30**, 577–582.

58 S. Koseki, N. Matsunaga, T. Asada, M. W. Schmidt and M. S. Gordon, *J. Phys. Chem. A*, 2019, **123**, 2325–2339.
59 J. F. Corbey, D. H. Woen, C. T. Palumbo, M. E. Fieser, J. W. Ziller, F. Furche and W. J. Evans, *Organometallics*, 2015, **34**, 3909–3921.
60 M. A. Angadol, D. H. Woen, C. J. Windorff, J. W. Ziller and W. J. Evans, *Organometallics*, 2019, **38**, 1151–1158.
61 S. A. Moehring and W. J. Evans, *Organometallics*, 2020, **39**, 1187–1194.